In Operando X-ray Absorption Fine Structure Studies of Polyoxometalate Molecular Cluster Batteries: Polyoxometalates as Electron Sponges

Heng Wang,[†] Shun Hamanaka,[†] Yoshio Nishimoto,[†] Stephan Irle,[†] Toshihiko Yokoyama,[‡] Hirofumi Yoshikawa,*[,†] and Kunio Awaga*[,†,§]

[†]Department of Chemistry and Research Center for Materials Science (RCMS), Nagoya University, Furo-cho, Chikusa-ku, Nagoya 464-8602, Japan

[‡]Institute for Molecular Science, Okazaki 444-8585, Japan

[§]Core Research for Evolutional Science and Technology (CREST), Furo-cho, Chikusa-ku, Nagoya 464-8602, Japan

S *Supporting Information*

ABSTRACT: We carried out in operando Mo K-edge X-ray absorption fine structure measurements on the rechargeable molecular cluster batteries (MCBs) of polyoxometalates (POMs), in which a Keggin-type POM, $[PMo_{12}O_{40}]^{3-}$, is utilized as a cathode active material with a lithium metal anode. The POM-MCBs exhibit a large capacity of ca. 270 (A h)/kg in a voltage range between $V = 4.0$ V and $V = 1.5$ V. X-ray absorption near-edge structure analyses demonstrate that all 12 Mo^{6+} ions in $[PMo_{12}O_{40}]^{3-}$ are reduced to Mo^{4+} in the discharging process. This means the formation of a super-reduced state of the POM, namely, $[PMo_{12}O_{40}]^{27-}$, which stores 24 electrons, and this electron number can explain the large capacity of the POM-MCBs. Furthermore, extended X-ray absorption fine structure analyses reveal the molecular structure of $[PMo_{12}O_{40}]^{27-}$, which is slightly reduced in size compared to the original $[PMo_{12}O_{40}]^{3-}$ and involves Mo^{4+} metal−metal-bonded triangles. Density functional theory calculations suggest that these triangles are formed because of the large number of additional electrons in the super-reduced state.
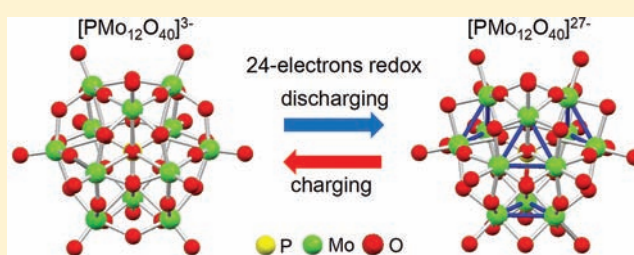
INTRODUCTION

Development of high-performance rechargeable batteries is one of the most important global issues to resolve the increasing environmental and energy concerns.[1,2] At present, lithium ion batteries (LIBs) are widely used for various portable electronic devices, such as mobile phones and laptop computers, due to their high energy densities.[3] However, the practical battery capacity of the LIBs is limited to less than ca. 50% of the theoretically possible value of the cathode active material, $LiCoO_2$, due to structural instabilities after the removal of Li^+ ions. In addition, the charging/discharging rate of the LIBs is slow, since this process includes the deintercalation/intercalation of lithium ions from/into the interlayer of CoO_2.[4] These drawbacks have motivated us to develop alternative cathode active materials for next-generation rechargeable batteries with high capacity and a rapid charging/discharging rate.[1,5−8]

Recently, we have proposed molecular cluster batteries (MCBs),[9−12] in which the cathode comprises polynuclear metal complexes (molecular clusters) and the anode is lithium metal. It is expected that MCBs would show a high capacity and a rapid charging/discharging due to multielectron redox reactions of the molecular clusters[13] and quick lithium ion diffusion, respectively.[12] In 2007, we prepared an MCB using an Mn_{12} cluster $([Mn_{12}O_{12}(CH_3COO)_{16}(H_2O)_4])$,[9] which is well-

known as a single-molecule magnet,[14] and found an extremely high discharging capacity of over 200 (A h)/kg, which was larger than those of the LIBs (ca. 148 (A h)/kg).[1,2] Furthermore, we carried out in situ Mn K-edge X-ray absorption fine structure (XAFS) analyses of the cathode materials in the Mn_{12}-MCBs to elucidate the solid-state electrochemical reactions in these batteries, because this spectroscopy is a powerful technique to determine the time evolution of both the local environment and valence of the metal ions.[15,16] This work revealed a super-reduction from $[Mn_{12}]^0$ to $[Mn_{12}]^{8-}$ in the discharging process,[10,11] which contributed to the high capacity.

Polyoxometalates (POMs) have attracted much attention due to their various properties, such as photoluminescence, catalytic activity, and single-molecule magnetism.[17] Their molecular structures can be regarded as nanoscale metal oxides from both structural and electronic points of view.[18] They are also reported to operate as a cathode active material of high-capacity lithium batteries,[19] though the valence and structural changes of the POMs in the battery reaction have not yet been investigated. In the present study, we performed in operando

Mo K-edge XAFS measurements on the MCBs of a representative Keggin-type POM, $TBA_3[PMo_{12}O_{40}]$ (TBA = $[N(CH_2CH_2CH_2CH_3)_4]^+$; see the inset of Figure 1) and found
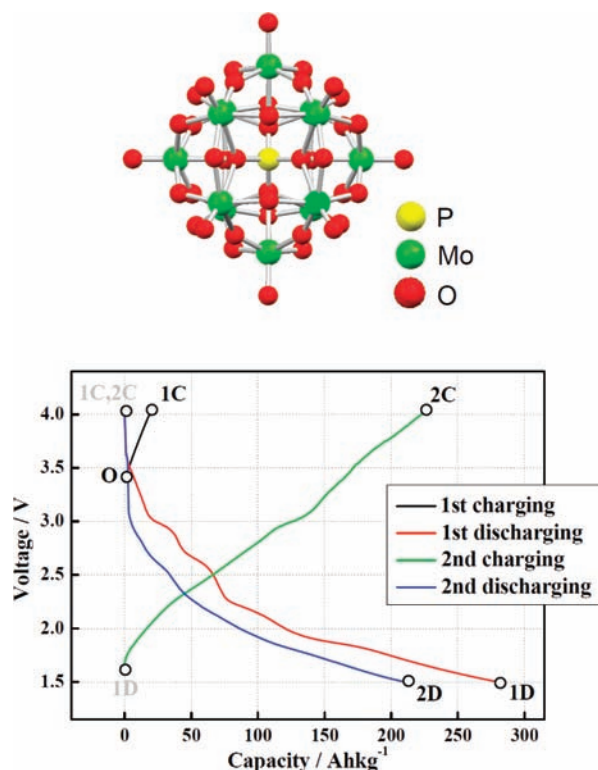
Figure 1. Charging and discharging curves of PMo_{12}/Li MCBs during XAFS measurements for first charging (black), first discharging (red), second charging (green), and second discharging (blue). **O**, **1C**, **1D**, **2C**, and **2D** indicate the characteristic samples in the first two cycles of the battery reaction. Inset: molecular structure of $[PMo_{12}]^{3-}$.

a 24-electron reduction in the discharging processes, which resulted in a high capacity of the POM-MCBs. Herein, we will describe the evolution of the redox states of the POM during charging/discharging and the possible molecular structure of the super-reduced species, $[PMo_{12}O_{40}]^{27-}$, in the fully discharged state.

■ EXPERIMENTAL SECTION

Battery Analyses of POM-MCBs. $TBA_3[PMo_{12}O_{40}]$ with a Keggin-type structure (see the inset of Figure 1) was synthesized according to the method described in the literature.[20] The cathode was prepared as follows: $TBA_3[PMo_{12}O_{40}]$, carbon black (Tokai Carbon), and poly(vinylidene fluoride) (Aldrich) were mixed at a weight ratio of 10:70:20, and then the slurry mixture was spread evenly with a thickness of 0.5 mm onto a polypropylene sheet and dried. The anode material was a lithium metal foil with a thickness of 0.2 mm. The cathode, anode, and separator (polyolefin film) were placed in a coin-shaped cell with an electrolyte, 1 M $LiPF_6$, in a mixed solution of ethylene carbonate (EC)/diethyl carbonate (DEC) (1:1, v/v) in an inert atmosphere. For in operando XAFS measurements, the battery was fabricated in a similar way using a special battery cell with an X-ray window in the center, which we developed previously (see Figure S1, Supporting Information).[11] The charging/discharging tests of the fabricated PMo_{12}/Li batteries were carried out at a constant current of 1.0 mA on a Hokuto HJ1001-SM8A charging/discharging device. The specific charging/discharging capacities were calculated on the basis of the weight of $TBA_3[PMo_{12}O_{40}]$, which was 10% of the weight of the cathode.

In Operando XAFS Measurements. In operando Mo K-edge XAFS spectra were recorded in the energy range from 19498.9 to 20003.9 eV in transmission mode at room temperature using the beamline BL-NW10A of the Photon Factory Advanced Ring (PF-AR) at KEK, Tsukuba, Japan. The in situ battery cell was placed between two transmission ion chambers. A Si(311) monochromator was used to select a specific X-ray energy. The intensities of the incident (I_0) and transmitted (I_t) X-rays were measured with ionization chambers filled with Ar and Kr, respectively. During in operando XAFS measurements, the area of the cathode subjected to the X-ray was ca. 1 mm^2. To avoid chemical decomposition of the POMs by X-ray, a quick XAFS (QXAFS) method was adapted, by which one spectrum was obtained within 60 s. During the charging/discharging reactions, we performed the measurements with an interval of 60 s. We also measured the QXAFS of the reference materials, Mo metal, and $TBA_3[PMo_{12}O_{40}]$, MoO_2, and Li_2MoO_4, which were diluted with boron nitride, using the same measurement conditions.

XAFS Data Analyses. X-ray absorption near-edge structure (XANES) spectra were obtained by pre-edge background subtraction with Victoreen-like functions and subsequent normalization using the software REX2000 (Rigaku Corp.).[21] Extended X-ray absorption fine structure (EXAFS) analyses were carried out by standard procedures using the analysis program EXAFSH written by Yokoyama et al.[22] The EXAFS oscillation function $k^3\chi(k)$ (k being the photoelectron wavenumber) was obtained by pre-edge baseline subtraction, postedge background estimation using cubic spline functions, and normalization with the atomic absorption coefficients. The employed k ranges in the Fourier transforms were approximately 2−12 $Å^{-1}$ for the Mo K-edge. Curve-fitting of in situ EXAFS data was performed by using the backscattering amplitudes and the phase shifts for appropriate Mo−O and Mo−Mo shells, which were calculated from the crystal structure of MoO_2[23] using the ab initio multiple-scattering code FEFF 8.4[24] or were obtained from the experimental EXAFS spectra of the reference materials, $TBA_3[PMo_{12}O_{40}]$ and Li_2MoO_4. Subsequently, the structural parameters, such as the coordination numbers (the number of neighboring atoms) and interatomic distances, were determined for Mo−O and Mo−Mo in the $[PMo_{12}O_{40}]^{3-}$ molecule during charging/discharging.

■ RESULTS AND DISCUSSION

Battery Performances of POM-MCBs. Although the battery performance of a $[PMo_{12}O_{40}]^{3-}$ salt is reported in ref 19, we re-examined it to confirm its high capacity, making a coin cell battery of $TBA_3[PMo_{12}O_{40}]$, in which the weight percentage of $TBA_3[PMo_{12}O_{40}]$ in the cathode was 10. Figure S2a (Supporting Information) shows the charge/discharge curves, measured at a constant load current of 1.0 mA in the voltage range of 1.5−4.2 V. In the first charging process (black curve), the voltage quickly increases from the initial value (ca. 3.4 V) to 4.2 V. It is likely that this pristine battery was nearly in a fully charged state. The first discharging (red curve) indicates a gradual voltage decrease and a high battery capacity of ca. 260 (A h)/kg at 1.5 V. This value is similar to the previously reported value for the POMs.[19] The second charging process (green) exhibits a gradual voltage increase to ca. 4.2 V, indicating a capacity of 250 (A h)/kg, which is nearly the same as that of the discharging process. The second discharging curve (blue) is very similar to the first one (red), and there is little decrease in capacity. Figure S2b shows the cycle performance of this POM-MCB up to the tenth run. There is no significant decrease in capacity; the value is maintained at ca. 210 (A h)/kg even in the last cycle, indicating that POMs are stable in the battery reactions.

In Operando XANES Analyses of POM-MCBs. We have developed a battery reaction cell for in operando XAFS studies, modifying a cell previously reported in the literature.[25] Figure 1

shows the charging/discharging curves of $[PMo_{12}O_{40}]^{3-}$ measured with this battery cell. A large capacity of ca. 270 (A h)/kg is obtained in the first discharging, as is found in the experiments with the coin cell.

The Mo K-edge XANES spectra were recorded during the battery reactions from the first charging to the second discharging (see Figure 1). The results are shown in Figure 2, in which the data are normalized to an edge step in the
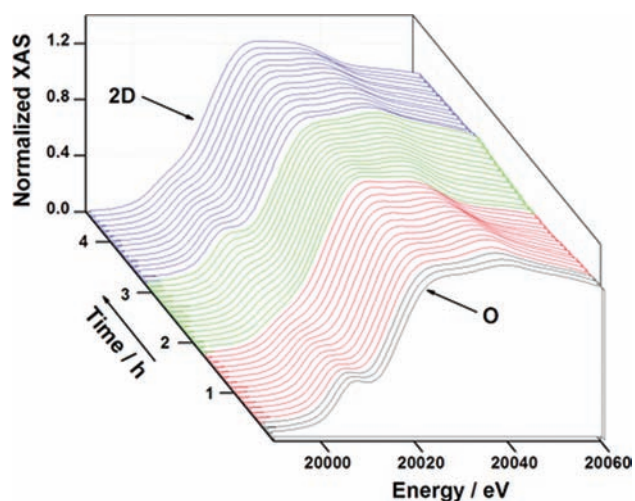

Figure 2. Normalized in operando Mo K-edge XANES spectra for first charging (black), first discharging (red), second charging (green), and second discharging (blue) of PMo_{12} MCBs during the first two cycles. See Figure 1 for a description of **O** and **2D**.

XANES energy region. The time trajectory indicates a systematic and reproducible change. Figure 3 shows the XANES spectra for the first discharging and second charging processes. There is a low-energy shift of the absorption curves during the discharging, while the curve returns to the original position after the charging. It is notable that these spectra indicate a shoulder around 20010 eV in the pre-edge region, which appears/disappears in the charging/discharging processes, respectively. This structure is well-known as a formally dipole forbidden excitation from 1s to 4d antibonding orbitals directed principally along the Mo=O bond.[26] Therefore, the appearance and disappearance of this structure in the battery reaction indicate the formation and elimination of the Mo=O bonds, respectively.

Mo K-edge XANES absorption edge energies have been utilized to determine the valence of molybdenum.[27] Figure S3 (Supporting Information) shows a linear relationship between the Mo oxidation state and the X-ray absorption edge energy for the reference materials, metal Mo, MoO_2, and $TBA_3[PMo_{12}O_{40}]$. As previously reported for XANES analyses of the other Mo materials,[27] the edge energy is defined as that at which the intensity reaches 60% of the absorption peak top. By using this relation, the averaged valence, Nv, of the Mo ions in the POM was calculated as shown in Figure 4, where the values of Nv are plotted as a function of the battery voltage V (see Figure 1). The lack of data in the second discharging is caused by an interruption of the incident X-ray due to a beam injection in PF-AR. The initial value of Nv before the first charging is ca. 6, which agrees with the fact that $[PMo_{12}O_{40}]^{3-}$ consists of 12 Mo^{6+} ions. This value exhibits no change during the first charging, which confirms that the as-prepared battery is in the charged state. In the first discharging, Nv exhibits a slight
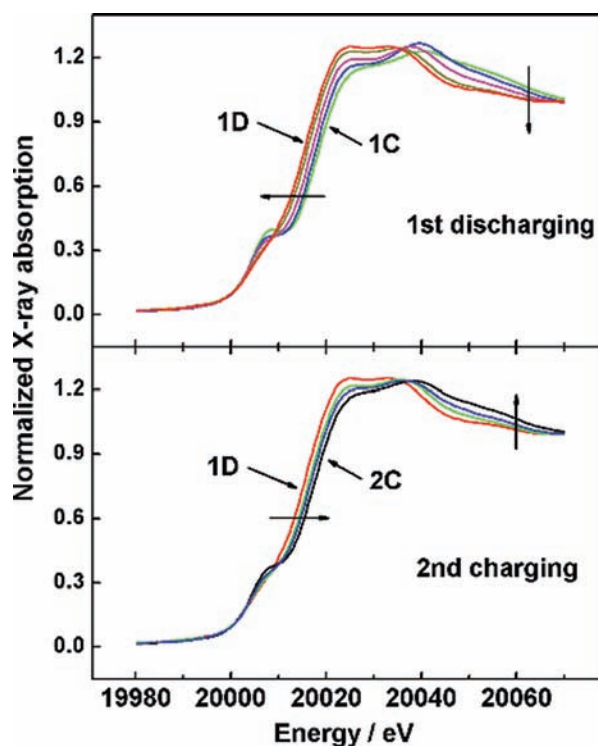
Figure 3. Mo K-edge XANES spectra for PMo_{12} MCBs in the first discharging and second charging. See Figure 1 for a description of **1C**, **1D**, and **2C**.
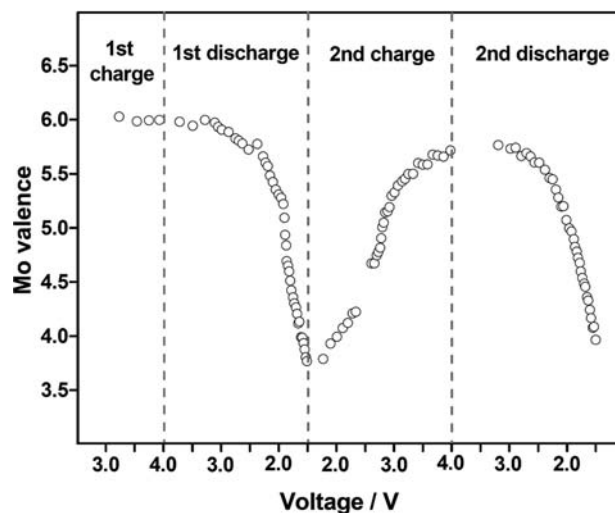
Figure 4. Averaged Mo valence of PMo_{12} in the PMo_{12} MCBs as a function of the cell voltage (V).

decrease from the initial value in the range of 4.0−3.0 V, which is consistent with the small capacity in this voltage range (see Figure 1). In the range of 3.0−1.5 V, however, Nv shows a quick decrease to 4.0. This voltage range of the valence change roughly agrees with the theoretical battery voltages (3.5−2.0 V) calculated from the redox potentials of $[PMo_{12}O_{40}]^{3-}$.[28] The second charging increases the value of Nv from 4.0 to 5.7, and the second discharging decreases it reversibly. The change in Nv by 2.0 during the discharging processes indicates that all 12 Mo^{6+} ions in the POM are reduced to Mo^{4+}; namely, one $[PMo_{12}O_{40}]^{3-}$ molecule can store 24 electrons. This value agrees with the observed battery capacity of ca. 270 (A h)/kg

(see Figure 1). Unlike in the usual LIBs, in which only half of the Co ions in $LiCoO_2$ are reduced, all the Mo ions can contribute to the battery capacity in the POM-MCBs.

The XANES analysis indicates that the reduction from Mo^{6+} to Mo^{4+} takes place at the 12 Mo^{6+} sites in one molecule in the range of 3.0–1.5 V, forming the super-reduced species, $[PMo_{12}O_{40}]^{27-}$, after the 24-electron reduction. In contrast, it is known that the usual solution electrochemistry can produce only two- or three-electron reduction species of $[PMo_{12}O_{40}]^{3-}$ in the typical electrochemical windows of solvents.[28] The solid-state electrochemistry of the POMs seems very different from the solution electrochemistry; e.g., the reduction of one Mo^{6+} site does not affect the other sites in the former. This is probably caused by the close contacts between the reduced sites and the counter cations (Li^+) and by a stabilization of the super-reduced species in a dielectric field of the solid.[29] $[PMo_{12}O_{40}]^{3-}$ can be regarded as a molecular "electron sponge," although this term has been used for the cobalt telluride clusters which exhibited only a two- or three-electron reduction.[30] Note that the formation of the super-reduced state is probably characteristic of the solid-state electrochemistry of molecular clusters, as an eight-electron reduction occurred for the Mn_{12} clusters in the Mn_{12}-MCBs.[11] Molecular clusters are promising cathode active materials for high-performance rechargeable batteries.

In Operando EXAFS Analyses of POM-MCBs. EXAFS analyses were performed for the POMs during charging and discharging to obtain structural information on this molecule. The $k^3\chi(k)$ functions for the experimentally obtained Mo absorption spectra are depicted in Figure S4 (Supporting Information). Figure 5 shows the Fourier transform (FT) spectra of the k^3-weighted data (the k range is around 2.0–12.0 $Å^{-1}$) for the samples denoted by **O**, **1C**, **1D**, **2C**, and **2D** in Figure 1. These spectra indicate the radial atomic distribution around Mo. The as-prepared sample **O** exhibits four main peaks at 1.1, 1.6, 2.3, and 3.2 Å, as indicated by the arrows. They have been assigned to a Mo=O double bond (1.7 Å), two kinds of Mo−O single bonds (1.9 and 2.4 Å), and a Mo−Mo distance (3.4 Å), respectively.[31] These distances are denoted in the molecular structure of $[PMo_{12}O_{40}]^{3-}$ (see Figures 1 and 6a).[32] The curve of **1C** is nearly the same as that of **O**. After the first discharging, however, **1D** exhibits a different spectrum; the peaks at 1.1 and 3.2 Å become very small, and those at 1.6 and 2.3 Å are significantly enhanced. After the second charging, sample **2C** exhibits the initial four peaks, though the peak at 3.2 Å becomes smaller in intensity and the peak at 1.6 Å becomes narrower in width, compared with those in **1C**. After the second discharging, the curve of **2D** is nearly the same as that of **1D**. This indicates a nearly reversible structural change of the POM molecule during the charging and discharging processes.

Figure 7 shows the evolution of the FT spectra in the first discharging (reduction) process from **1C** to **1D**. It is clear that the peaks at 1.1 and 3.2 Å swap intensities with those at 1.6 and 2.3 Å as the voltage V decreases from 4.0 V. The intensity decrease of the peak at 1.1 Å and the increase at 1.6 Å are ascribed to the transformation from a Mo=O double bond to a Mo−O single bond, as also indicated by the XANES spectra for the discharging process (see Figure 2). The other intensity swapping between the peaks at 3.2 and 2.3 Å is probably caused by a shortening of the Mo−Mo distance, as described later.

We carried out curve-fitting for the in operando EXAFS spectra using the parameters of the backscattering amplitudes and the phase shifts of the appropriate Mo−O and Mo−Mo
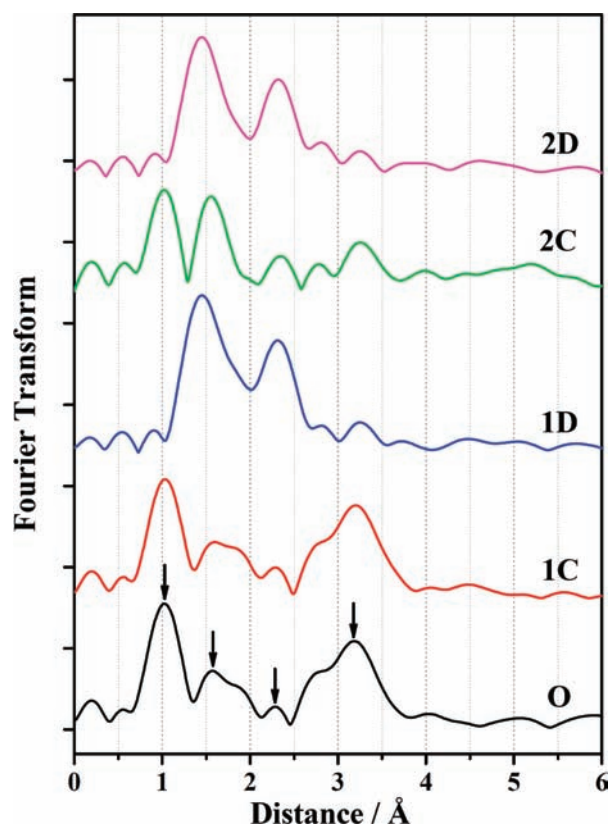

Figure 5. Experimental Fourier transforms of the Mo K-edge EXAFS spectra for **O**, **1C**, **1D**, **2C**, and **2D**. The arrows in **O** indicate the peaks used in EXAFS analyses. See Figure 1 for a description of **O**, **1C**, **1D**, **2C**, and **2D**.

shells, which were obtained from the reference materials, MoO_2 and $TBA_3[PMo_{12}O_{40}]$. The Mo−O peak at 1.6 Å was analyzed by using two Mo−O shells with distances of 1.9 and 2.0 Å (see Table S1, Supporting Information), while the other peaks were analyzed by the one-shell model. The coordination numbers
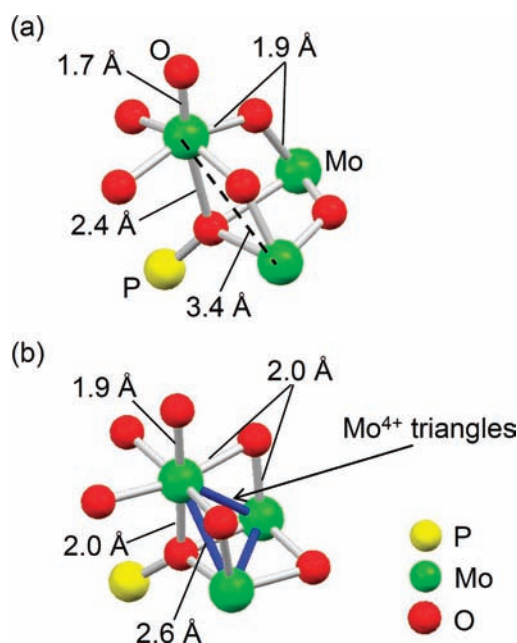
Figure 6. Local structures of (a) $[PMo_{12}]^{3-}$ and (b) $[PMo_{12}]^{27-}$.
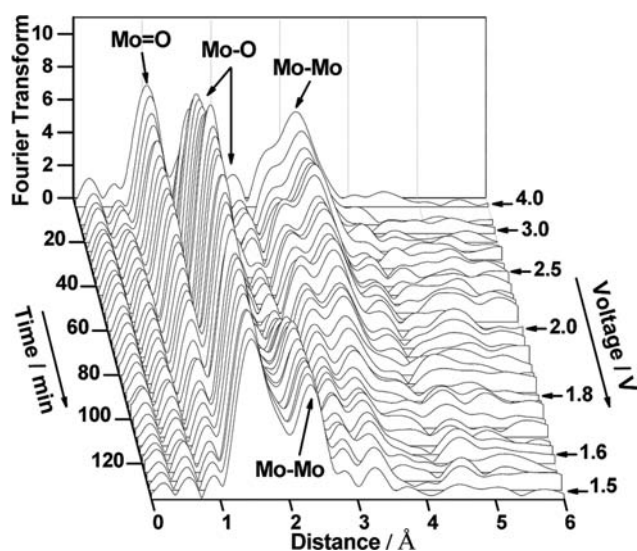
Figure 7. Evolution of the Fourier transforms of the Mo K-edge EXAFS spectra in the first discharge.

and interatomic distances were obtained as fitting variables for all the shells used in the curve-fittings, while the Debye–Waller factors and the energy shifts E were fixed. The results are shown in Table S1 for **O**, **1C**, **1D**, **2C**, and **2D**. Figure S5 (Supporting Information) shows the evolution of all the interatomic distances obtained by this curve-fitting. These interatomic distances exhibit no significant changes. Figure S6 (Supporting Information) shows the evolution of the coordination numbers for the shells in the first discharging and second charging. The data are rather scattered, presumably because the cathode becomes inhomogeneous during the charging/discharging, but the obtained coordination number can be a good indicator for the number of neighboring atoms. Actually, the summation of the coordination numbers for all the M=O and M–O shells in **O** and **1C** becomes ca. 6, which is consistent with six-coordinated Mo (see Table S1). As shown in Figure S6a,b, the summation of the coordination numbers for the Mo–O shells (1.9 and 2.0 Å) slightly increases during the discharging, while those for Mo=O (1.7 Å) and Mo–O (2.4 Å) approach 0. These tendencies imply that all the Mo–O interatomic distances become ca. 2.0 Å, accompanied by the disappearance of Mo=O. Figure S6c indicates the evolution of the coordination numbers for two kinds of Mo–Mo distances. In the discharging process, the coordination number for the Mo–Mo distance of 3.4 Å decreases, while that for 2.6 Å increases. These results suggest that the Mo–Mo distance shortens from 3.4 to 2.6 Å; that is, the Mo(IV)–Mo(IV) bond is formed in the reduction species of the POM during battery discharging.

Model Structure of the 24-Electron-Reduced POM. The EXAFS analysis suggested that the distances of Mo–O and Mo–Mo become ca. 2.0 and 2.6 Å, respectively, after discharging. By taking into account these changes from the original $[PMo_{12}O_{40}]^{3-}$ structure (see Figure 8a), we estimated the local structure of the 24-electron-reduced POM molecule, $[PMo_{12}O_{40}]^{27-}$, on the basis of density functional theory (DFT) calculations, as detailed in the Supporting Information and as shown in Figure 6b. In this structure, all the Mo–O distances are set to be 1.9–2.0 Å, and the nearest Mo–Mo distance is fixed at 2.6 Å to make a metal–metal single bond. Assuming that the $[PMo_{12}O_{40}]^{27-}$ molecule has the highest
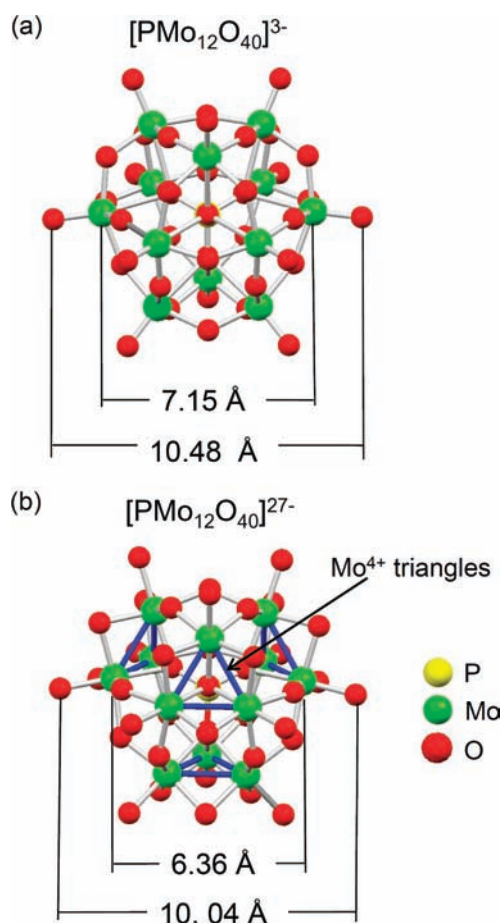

Figure 8. (a) Molecular structure of $[PMo_{12}]^{3-}$ and (b) model molecular structure of $[PMo_{12}]^{27-}$.

symmetry, we constructed a model structure by assembling the local structure in Figure 6b, as shown in Figure 8b. This structure is slightly reduced in size from the original one; the maximum dimension of the $[PMo_{12}O_{40}]^{3-}$ decreases from 10.5 to 10.0 Å (see Figure 8). In addition, this structure involves a characteristic triangular structure formed by Mo^{4+} metal–metal bonding, which corresponds to the frontier molecular orbitals found in the DFT calculations. These results suggest that these triangles are formed due to the large number of additional electrons in the super-reduced state. The structural feature of $[PMo_{12}O_{40}]^{27-}$ is similar to a partial structure of MoO_2 including a Mo–Mo single bond.[23] Herein, using the expected structure of $[PMo_{12}O_{40}]^{27-}$, we simulated the EXAFS spectra of this molecule by using the backscattering amplitudes and the phase shifts for appropriate Mo–O and Mo–Mo shells. They are calculated from the model structure in Figure 8 using the ab initio multiple-scattering code FEFF 8.4.[24] The simulated EXAFS spectrum is shown in Figure 9 with the experimental spectrum for the fully discharged state (**1D**). The simulation can reproduce the features of the experimental spectrum very well. It is thus highly probable that the model structure explains the structure of $[PMo_{12}O_{40}]^{27-}$. Theoretical studies are in progress to elucidate the stability of this structure.

■ CONCLUSIONS

In operando Mo K-edge XAFS measurements on POM-MCBs revealed the evolution of the oxidation state and the local structure of Mo ions of the $[PMo_{12}O_{40}]^{3-}$ molecule in the
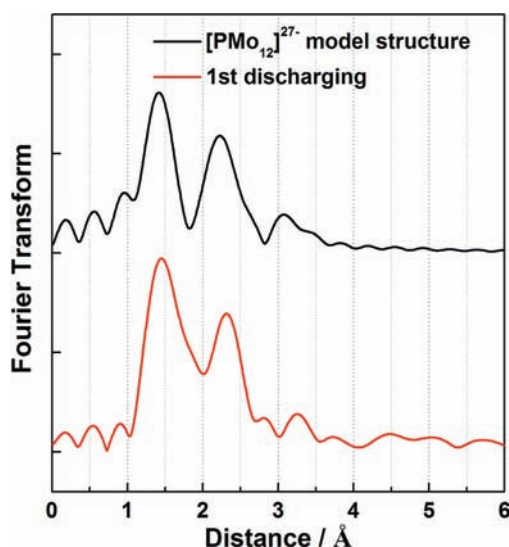
Figure 9. Experimental Mo K-edge EXAFS spectra for **1D** and simulated Mo K-edge EXAFS spectra for the $[PMo_{12}]^{27-}$ model structure.

battery reaction. $[PMo_{12}O_{40}]^{3-}$ exhibited a reversible 24-electron redox during charging/discharging, which resulted in a large capacity, and the structure of $[PMo_{12}O_{40}]^{27-}$ was proposed by a slight shrinkage in molecular size from $[PMo_{12}O_{40}]^{3-}$. These results suggest that the solid-state electrochemistry of the battery reactions enables the formation of the highly reduced species. This electron sponge behavior is a newly revealed characteristic of POMs and indicates that they are promising cathode active materials for high-performance rechargeable batteries.

■ ASSOCIATED CONTENT

Ⓢ Supporting Information

Schematic sketch of the in situ cell, coin cell battery performances, Mo K-edge XANES spectra for the reference materials, Mo valence vs energy plots for the reference materials, Mo K-edge EXAFS functions of $k^3\chi(k)$ for **O**, **1C**, **1D**, **2C**, and **2D**, evolution of interatomic distances and coordination numbers obtained from EXAFS analyses, and computational details on DFT calculations. This material is available free of charge via the Internet at http://pubs.acs.org.

■ AUTHOR INFORMATION

Corresponding Author
yoshikawah@chem.nagoya-u.ac.jp; awaga@mbox.chem.nagoya-u.ac.jp

Notes
The authors declare no competing financial interest.

■ ACKNOWLEDGMENTS

■ REFERENCES

(1) Armand, M.; Tarascon, J. -M. *Nature* **2008**, *451*, 652−657.
(2) Tarascon, J. -M.; Armand, M. *Nature* **2001**, *414*, 359−367.
(3) Manthiram, A. *NATO Sci. Ser. II* **2002**, *61*, 157−175.

(4) Linden, D.; Reddy, T. B. *Handbook of Batteries*, 3rd ed.; McGraw-Hill: New York, 2002.
(5) Nakahara, K.; Oyaizu, K.; Nishide, H. *Chem. Lett.* **2011**, *40*, 222−227.
(6) Nigrey, P. J.; MacInnes, D. Jr.; Nairns, D. P.; MacDiarmid, A. G.; Heeger, A. J. *J. Electrochem. Soc.* **1981**, *128*, 1651−1654.
(7) Visco, S. J.; Liu, M.; De Jonghe, L. C. *J. Electrochem. Soc.* **1990**, *137*, 1191−1192.
(8) Nguyen, T. L. A.; Demir-Cakan, R.; Devic, T.; Morcrette, M.; Ahnfeldt, T.; Auban-Senzier, P.; Stock, N.; Goncalves, A.-M.; Filinchuk, Y.; Tarascon, J.-M.; Fèrey, G. *Inorg. Chem.* **2010**, *49*, 7135−7143.
(9) Yoshikawa, H.; Kazama, C.; Awaga, K.; Satoh, M.; Wada, J. *Chem. Commun.* **2007**, *43*, 3169−3170.
(10) Yoshikawa, H.; Hamanaka, S.; Miyoshi, Y.; Kondo, Y.; Shigematsu, S.; Akutagawa, N.; Sato, M.; Yokoyama, T.; Awaga, K. *Inorg. Chem.* **2009**, *48*, 9057−9059.
(11) Wang, H.; Hamanaka, S.; Yokoyama, T.; Yoshikawa, H.; Awaga, K. *Chem.—Asian. J.* **2011**, *6*, 1074−1079.
(12) Kawasaki, N.; Wang, H.; Nakanishi, R.; Hamanaka, S.; Kitaura, R.; Shinohara, H.; Yokoyama, T.; Yoshikawa, H.; Awaga, K. *Angew. Chem., Int. Ed.* **2011**, *50*, 3471−3474.
(13) Sessoli, R.; Tsai, H. −L.; Schake, A. R.; Wang, S.; Vincent, J. B.; Folting, K.; Gatteschi, D.; Christou, G.; Hendrickson, D. N. *J. Am. Chem. Soc.* **1993**, *115*, 1804−1816.
(14) Caneschi, A.; Gatteschi, D.; Sessoli, R.; Barra, A. L.; Brunel, L. C.; Guillot, M. *J. Am. Chem. Soc.* **1991**, *113*, 5873−5874.
(15) Islame, M. S.; Ammundsen, B.; Jones, D. J.; Roziere, J. In *Materials for Lithium-Ion Batteries*; Julien, C., Stoynov, Z., Eds.; Academic Press: Amsterdam, The Netherlands, 2000; p 279.
(16) Braun, A.; Shrout, S.; Fowlks, A. C.; Osaisai, B. A.; Seifert, S.; Granlund, E.; Cairns, J. *J. Synchrotron Radiat.* **2003**, *10*, 320−325.
(17) (a) Long, D.-L.; Tsunashima, R.; Cronin, L. *Angew. Chem., Int. Ed.* **2010**, *49*, 1736−1758. (b) Long, D.-L.; Burkholder, E.; Cronin, L. *Chem. Soc. Rev.* **2007**, *36*, 105−121. (c) Hill, C. L. *Chem. Rev.* **1998**, *98*, 1−2. (d) Binnemans, K. *Chem. Rev.* **2009**, *109*, 4283−4374. (e) Pope, M. T.; Muller, A. *Angew. Chem., Int. Ed. Engl.* **1991**, *30*, 34−48. (f) Kozhevnikov, I. V. *Chem. Rev.* **1998**, *98*, 171−198. (g) Compain, J.-D.; Mialane, P.; Dolbecq, A.; Mbomekalle, I. M.; Marrot, J.; Secheresse, F.; Riviere, E.; Rogez, G.; Wernsdorfer, W. *Angew. Chem., Int. Ed.* **2009**, *48*, 3077−3081. (h) Fleming, C.; Long, D.-L.; McMillan, N.; Johnston, J.; Bovet, N.; Dhanak, V.; Gadegaard, N.; Kögerler, P.; Cronin, L.; Kadodwala, M. *Nat. Nanotechnol.* **2008**, *3*, 229−333.
(18) Pope, M. T. *Heteropoly and Isopoly Oxometalates*; Springer-Verlag: Berlin, 1983.
(19) (a) Cantu, M. L.; Romero, P. G. *Chem. Mater.* **1998**, *10*, 698−704. (b) Azumi, B. M.; Ishihara, T.; Nishiguchi, H.; Takita, Y. *Electrochemistry* **2002**, *70*, 869−874.
(20) Sanchez, C.; Livage, J.; Launay, J. P.; Fournier, M.; Jeannin, Y. *J. Am. Chem. Soc.* **1982**, *104*, 3194−3202.
(21) Taguchi, T.; Ozawa, T.; Yashiro, H. *Phys. Scr.* **2005**, *T115*, 205−206.
(22) Yokoyama, T.; Hamamtsu, H.; Ohta, T. *EXAFSH Version 2.1, EXAFS Analysis Program*; The University of Tokyo: Tokyo, 1994.
(23) Eyert, V.; Horny, R.; Hock, K.-H.; Horn, S. *J. Phys.: Condens. Matter* **2000**, *12*, 4923−4946.
(24) Ankudinov, A. L.; Ravel, B.; Rehr, J. J.; Conradson, S. D. *Phys. Rev. B* **1998**, *58*, 7565−7576.
(25) Braun, A.; Shrout, S.; Fowlks, A. C.; Osaisai, B. A.; Seifert, S.; Granlund, E.; Cairns, J. *J. Synchrotron Radiat.* **2003**, *10*, 320−325.
(26) (a) Jalilehvand, F.; Lim, B. S.; Holm, R. H.; Hedman, B.; Hodgson, K. O. *Inorg. Chem.* **2003**, *42*, 5531−5536. (b) Shiju, N. R.; Rondinone, A. J.; Mullins, D. R.; Schwartz, V.; Overbury, S. H.; Guliants, V. V. *Chem. Mater.* **2008**, *20*, 6611−6616.
(27) (a) Berry, A. J.; Yaxley, G. M.; Woodland, A. B.; Foran, G. J. *Chem. Geol.* **2010**, *278*, 31−37. (b) Macias, B.; Malet, P.; Paradinas, R.; Rives, V.; Villa, M. V. *Inorg. Chim. Acta* **1999**, *288*, 127−133. (c) Safonova, O. V.; Deniau, B.; Millet, J.-M. M. *J. Phys. Chem. B* **2006**,

110, 23962−23967. (d) Wienold, J.; Timpe, O.; Ressler, T. *Chem.—Eur. J.* **2003**, *9*, 6007−6017.

(28) Maeda, K.; Himeno, S.; Osakai, T.; Saito, A.; Hori, T. *J. Electroanal. Chem.* **1994**, *364*, 149−154.

(29) Zhao, L.; Xu, Z. Q.; Grove, H.; Milway, V. A.; Dawe, L. N.; Abedin, T. S. M.; Thompson, L. K.; Kelly, T. L.; Harvey, R. G.; Miller, D. O.; Weeks, L.; Shapter, J. G.; Pope, K. J. *Inorg. Chem.* **2004**, *43*, 3812−3824.

(30) (a) Brunner, H.; Cattey, H.; Meier, W.; Mugnier, Y.; Stückl, A. C.; Wachter, J.; Wanninger, R.; Zabel, M. *Chem.—Eur. J.* **2003**, *9*, 3796−3802. (b) Bencharif, M.; Cador, O.; Cattey, H.; Ebner, A.; Halet, J.-F.; Kahlal, S.; Meier, W.; Mugnier, Y.; Saillard, J.-Y.; Schwarz, P.; Trodi, F. Z.; Wachter, J.; Zabel, M. *Eur. J. Inorg. Chem.* **2008**, 1959−1968.

(31) Wienold, J.; Timpe, O.; Ressler, T. *Chem.—Eur. J.* **2003**, *9*, 6007−6017.

(32) Liu, S.; Wang, C.; Zhai, H.; Li, D. *J. Mol. Struct.* **2003**, *654*, 215−221.